Earth and Planetary Science Letters 493 (2018) 92–101

Contents lists available at ScienceDirect

Earth and Planetary Science Letters

www.elsevier.com/locate/epsl

Biolabile ferrous iron bearing nanoparticles in glacial sediments

Jon R. Hawkings [a,*], Liane G. Benning [b,c,d], Rob Raiswell [c], Burkhard Kaulich [e], Tohru Araki [e], Majid Abyaneh [e], Anthony Stockdale [c], Monika Koch-Müller [b], Jemma L. Wadham [a], Martyn Tranter [a]

[a] Bristol Glaciology Centre, School of Geographical Sciences, University of Bristol, University Road, Bristol, BS8 1SS, UK
[b] German Research Center for Geosciences GFZ, Telegrafenberg, Department 4, 14473, Potsdam, Germany
[c] Cohen Lab, School of Earth and Environment, Maths/Earth and Environment Building, University of Leeds, Leeds, LS2 9JT, UK
[d] Department of Earth Sciences, Free University of Berlin, 12249 Berlin, Germany
[e] Diamond Light Source, Diamond House, Harwell Science and Innovation Campus, Didcot, Oxfordshire, OX11 0DE, UK

ARTICLE INFO

Article history:
Received 9 October 2017
Received in revised form 12 April 2018
Accepted 14 April 2018
Available online 25 April 2018
Editor: D. Vance

Keywords:
glaciers
Arctic
iron
biological pump
export-productivity
sediment

ABSTRACT

Glaciers and ice sheets are a significant source of nanoparticulate Fe, which is potentially important in sustaining the high productivity observed in the near-coastal regions proximal to terrestrial ice cover. However, the bioavailability of particulate iron is poorly understood, despite its importance in the ocean Fe inventory. We combined high-resolution imaging and spectroscopy to investigate the abundance, morphology and valence state of particulate iron in glacial sediments. Our results document the widespread occurrence of amorphous and Fe(II)-rich and Fe(II)-bearing nanoparticles in Arctic glacial meltwaters and iceberg debris, compared to Fe(III)-rich dominated particulates in an aeolian dust sample. Fe(II) is thought to be highly biolabile in marine environments. Our work shows that glacially derived Fe is more labile than previously assumed, and consequently that glaciers and ice sheets are therefore able to export potentially bioavailable Fe(II)-containing nanoparticulate material to downstream ecosystems, including those in a marine setting. Our findings provide further evidence that Greenland Ice Sheet meltwaters may provide biolabile particulate Fe that may fuel the large summer phytoplankton bloom in the Labrador Sea, and that Fe(II)-rich particulates from a region of very high productivity downstream of a polar ice sheet may be glacial in origin.

1. Introduction

Iron (Fe) is an essential micronutrient for marine phytoplankton, and its availability limits growth of primary producers in large parts of the world's oceans (Moore et al., 2013). Fe availability is therefore critical in dictating the strength of the ocean biological pump, which in turn affects atmospheric CO_2 concentrations and global climate (Moore et al., 2013). A critical control on the availability of iron in seawater is its solubility. In oxygenated waters, the more reactive and soluble ferrous oxidation state, Fe(II), readily oxidises to the ferric state, Fe(III), which is poorly soluble. Dissolved Fe^{2+} is more labile than Fe^{3+} in oxic environments, where it is thermodynamically unstable unless stabilised by organic colloids (Breitbarth et al., 2009; Lam et al., 2012). The majority of available iron in the oceanic euphotic zone is consequently thought to exist as nanoparticulate/colloidal Fe(III), varying in size, speciation and structure, and therefore in solubility and bioavailability (Raiswell and Canfield, 2012; von der Heyden et al., 2014). However, recent studies suggest that a particulate Fe(II) pool may play a significant role (Lam et al., 2012; von der Heyden et al., 2012). The speciation and minerology of Fe particulates appears particularly important in dictating bioavailability (Lam et al., 2012; Shaked and Lis, 2012; von der Heyden et al., 2012; Shoenfelt et al., 2017). Currently our understanding of the valence state of potentially bioavailable Fe sources in the ocean is limited due to measurement challenges (von der Heyden et al., 2012).

Glaciers and ice sheets are large sources of iron to the polar oceans, principally via iceberg rafted debris (Death et al., 2014; Duprat et al., 2016; Raiswell et al., 2016) and meltwater runoff (Schroth et al., 2011; Gerringa et al., 2012; Bhatia et al., 2013; Hawkings et al., 2014; Lyons et al., 2015; Hodson et al., 2017). Most potentially bioavailable Fe is delivered as poorly ordered oxyhydroxide nanoparticles, primarily ferrihydrite, which were identified by high resolution transmission electron microscopy (HR-TEM) and sediment extractions (Raiswell, 2011; Hawkings et al., 2014; Raiswell et al., 2016). Particulate Fe, especially ferrihydrite, has

* Corresponding author.
E-mail address: jon.hawkings@bristol.ac.uk (J.R. Hawkings).

https://doi.org/10.1016/j.epsl.2018.04.022

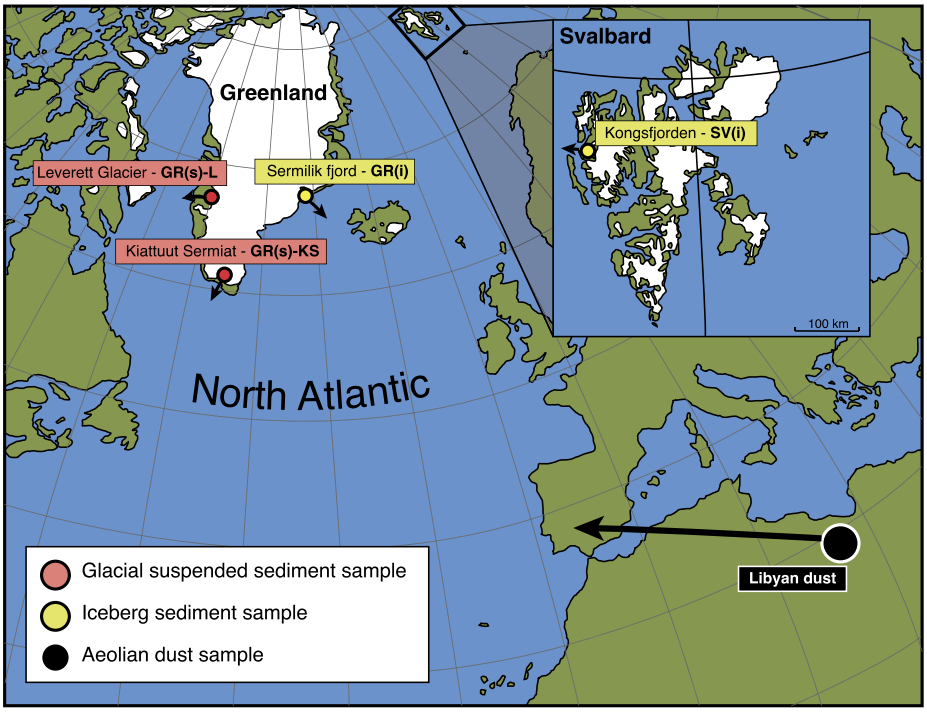

Fig. 1. Map of sample locations and source type. Two suspended sediment samples (red dots) and one iceberg sample (yellow dot) were collected from the Greenland Ice Sheet. One additional iceberg sample was collected from Kongsfjorden in Svalbard (insert, yellow dot). An aeolian dust precursor sample was also collected from Libya (black dot). This sample was also treated to simulate cloud-processing effects (Shi et al., 2012). Arrows indicate approximate path of transport to the ocean. GR = Greenland, SV = Svalbard. (For interpretation of the colours in the figure(s), the reader is referred to the web version of this article.)

already been demonstrated to be, at least to some degree, bioavailable to phytoplankton cultures (Smith et al., 2007; Raiswell and Canfield, 2012; Sugie et al., 2013; Shoenfelt et al., 2017). Glacial sediments may contain a range of particulate iron species, including a particulate and extractable Fe(II) component (Hopwood et al., 2014; Shoenfelt et al., 2017). Particulate Fe in marine waters around the Antarctic coastline has a distinctive Fe(II) dominated mineralogy associated with a region of very high primary productivity in the Southern Ocean (von der Heyden et al., 2012). In addition, Antarctic ice streams have been postulated to channel subglacial meltwaters from the continental interior to the coastal ocean (Le Brocq et al., 2013; Garabato et al., 2017), the fluxes of which may be elevated during glacial periods (Frisia et al., 2017). These meltwaters may be anoxic in places and contain high concentrations of Fe(II) (Wadham et al., 2013) that may be exported downstream in dissolved or (nano)particulate form to near coastal ecosystems (Annett et al., 2017). Thus, highly reactive Fe(II) bearing particles may originate from glacial input and may be stabilised via binding to inorganic or organic ligands (von der Heyden et al., 2012), which makes them an important source of potentially bioavailable Fe to marine biota.

Evidence for the export of biolabile Fe(II) particles from ice sheets is lacking, but here we have quantified the nanoscale mineralogical and spectroscopic characteristics of Arctic glacial meltwater suspended sediments and iceberg rafted debris. We determined the distribution and speciation of particulate Fe at high-resolution (30–50 nm/pixel) using synchrotron scanning X-ray microscopy (SXM), complemented by high resolution transmission electron microscopy (HR-TEM), energy-dispersive X-ray spectroscopy (EDS) and electron energy loss spectroscopy (EELS) analyses. These analytical tools allowed us to assess the variations in the oxidation state and coordination environments of complex particles to determine the form of nanoparticulate Fe present, which influences its solubility and bioavailability. We show that glacially derived iron nanoparticles have a distinct speciation that suggests high bioavailability.

2. Methods

2.1. Sample source regions

Samples were collected from four glacial locations in the northern polar region, and one dust source to the North Atlantic (Fig. 1). The two suspended sediment samples were collected near the terminus of Leverett Glacier in southwest Greenland (GR(s)-L; 67.06°N, 50.17°W) and Kiattuut Sermiat in Southern Greenland (GR(s)-KS; 61.21°N, 45.33°W) (Hawkings et al., 2016), during May 2012 and June 2013 respectively. Both glaciers drain the Greenland Ice Sheet, but Leverett Glacier has a significantly larger hydrologically active catchment area (~600 km^2 vs ~36 km^2; Hawkings et al., 2016). One iceberg sediment sample was collected in Sermilik fjord, East Greenland (GR(i); 65.7°N, 37.9°W) in July 2014, and the other from Kongsfjorden in Svalbard (SV(i); 78.9°N, 12.1°E) in July 2013. These were compared to a precursor aeolian dust sample collected from Libya, and the precursor aeolian dust after simulated low-pH atmospheric processing (Shi et al., 2015). The Libyan dust precursor sample was collected from the Tibesti Mountains in South Libya, Western Sahara (23.6°N, 16.5°E; detailed description available in Shi et al., 2011).

2.2. Sample collection

Glacial meltwater and iceberg samples were collected by filtration onto a 0.4 µm polycarbonate (Whatman Cyclopore®) or 0.45 µm cellulose nitrate filter (Whatman®) as detailed elsewhere (Hawkings et al., 2014; Raiswell et al., 2016). Meltwater samples were collected in lab detergent and acid-washed 1,000 mL bottles (1% DECON for 24 h, 3× rinsed 18.2 $M\Omega\,cm^{-1}$ de-ionised water, 10% HCl for 24 h, then 6× rinsed with 18.2 $M\Omega\,cm^{-1}$ de-ionised water and dried in a laminar flow hood; Nalgene™ low density polyethylene). Meltwater samples were taken from a flowing section of the main river channel and filtered within 15–30 min of collection inside a designated clean lab tent or field hut (Hawkings et al., 2014, 2016). Iceberg samples were collected from a boat,

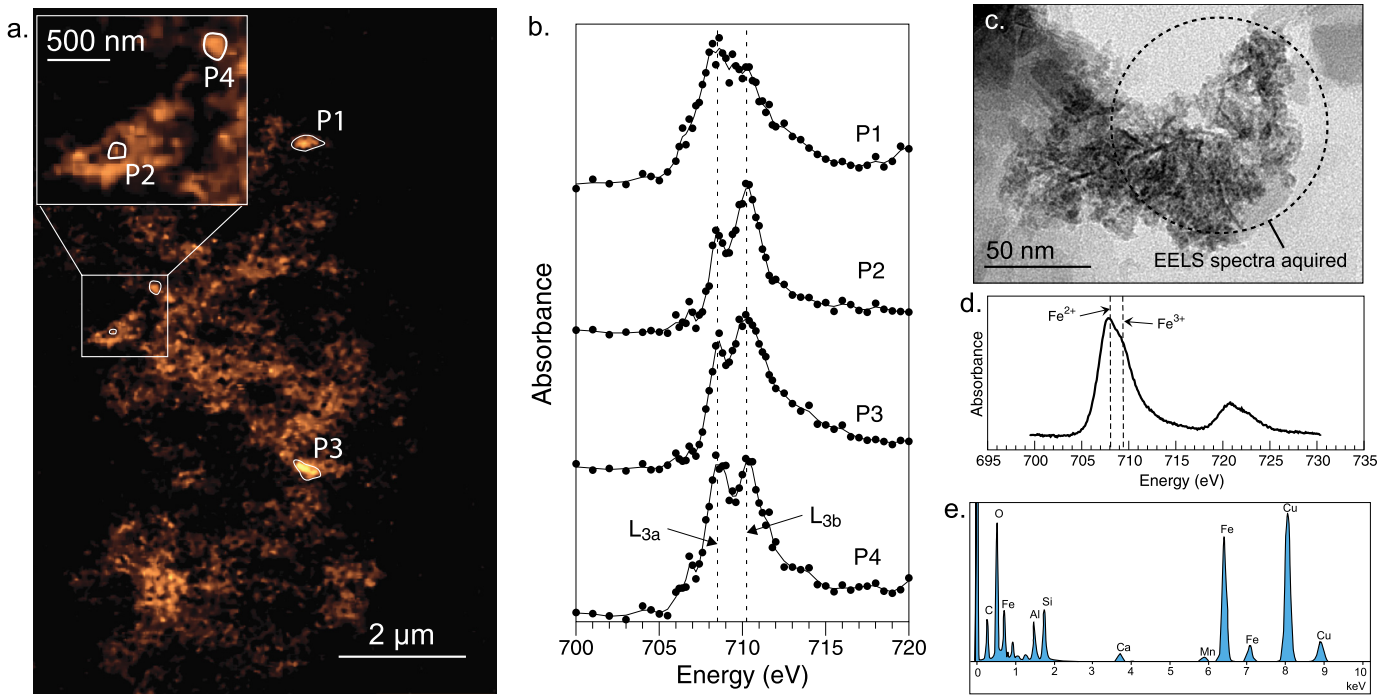

Fig. 2. **(a)** Distribution of Fe in a particle aggregate from GR(s)-L sample generated by subtracting the signal at 710 eV from 705 eV. **(b)** XANES spectra associated with Fe-rich regions identified in **(a)**. Spectra were acquired from 700–720 eV at a spectral resolution of 0.1–1 eV, with higher resolution closer the Fe L_3-edge, a dwell time of 2 ms and a spatial resolution of 30–50 nm/pixel. L_{3a} represents the Fe(II) peak, and L_{3b} the Fe(III) peak. **(c)** HR-TEM photomicrograph of nanoparticulate Fe-rich material from the same sample, **(d)** associated EELS spectra and **(e)** EDS spectra of the Fe-rich region indicated in **(c)** with Fe(II) and Fe(III) peaks identified in **(d)**. Fitting of the EELS spectra (van Aken and Liebscher, 2002) in **(d)** demonstrated a high proportion of Fe(II) present (~66% Fe(II); Fig. 5b).

with a clean ice axe into a new polyethylene bag. The outer layer of ice was allowed to melt and was subsequently discarded before the remaining ice was transferred into a new polyethylene bag and allowed to melt completely before immediate filtration (Raiswell et al., 2016). Approximately 200–1,000 mL of meltwater was vacuum filtered through a 47 mm membrane mounted onto a polysulfone filter holder with receiver (Nalgene™), until the filter was blocked (the filtration rate being extremely slow). The filter membrane was removed from the filter stack using tweezers and placed folded into a zip lock bag, after a few minutes under vacuum to gently air dry. Coarse material (>~1 mm in size) was removed using tweezers before storage, for coarser iceberg sediments. The aeolian dust sample was collected from the source using a spatula and plastic microcentrifuge tube. Glacial samples were stored air dried and refrigerated on filters (for a maximum of three years before analysis), and dust samples were stored freeze-dried at room temperature (for a maximum of ten years before analysis), in accordance with studies of iron (oxy)hydroxide stability (Raiswell et al., 2010). At 4 °C the half-life of the most reactive iron (oxy)hydroxide, ferrihydrite, is ~1500 days in a water suspension (Schwertmann et al., 2004), unless complexed with organic or inorganic ions (Raiswell and Canfield, 2012), therefore we anticipate little alteration of our samples over this time period. The aeolian dust precursor has been exposed to subaerial weathering for a long-time period before collection and therefore dry storage for several years is likely insignificant for oxidation artifacts. The dust precursor was size fractionated using a dust tower (Shi et al., 2011, 2012) and only the <10 µm fraction was used.

2.3. Processed Aeolian dust sample

We analysed the precursor dust sample after simulated cloud processing, following the procedure by Shi et al. (2015). Briefly, ~60 mg of dust was exposed to 1 L of pH 1 H_2SO_4 solution, continuously stirred for ~72 h. The solution was then adjusted to pH 5–6 using ammonium hydroxide, and the dust isolated into a plastic microcentrifuge tube after rinsing with ultra-pure deionised water (Milli-Q; 18.2 MΩ cm^{-1}) and drying.

2.4. SXM analysis

Samples were prepared for SXM analysis at the Diamond Light Source (UK) I08 beamline lab over a five-day period. A few milligrams of sample was placed in a microcentrifuge tube, and dispersed in ethanol in an ultrasonic bath. The 6-line ferrihydrite and pyrite standard samples were prepared in identical fashion for analysis. A small quantity of sample was pipetted onto a silicon nitride membrane and mounted on the beamline. We first imaged and spectrally mapped larger (~30 × 30 $µm^2$) areas at a resolution of 250–500 nm/pixel to identify regions (~2–3 $µm^2$) with particles for subsequent collection of Fe μ-XANES image stacks, in each sample. Subsequently, 3–10 regions of interest (ROI; ~2–3 $µm^2$) were identified using Fe intensity maps (705 eV *vs.* 710 eV) for further analysis of particulate Fe speciation. The ROI were raster-scanned with a dwell time of 2 ms and a spatial resolution of 30–50 nm/pixel, and a stack of images over the full Fe L-edge from 700 eV to 720 eV, at a spectral resolution of 0.2–1 eV (with higher resolution closer to the Fe L-edge), were acquired over a 16–24 h scan period.

Analyses were conducted at particle scale, although X-ray absorption near-edge structure (XANES) spectra were collected for each pixel (e.g. Fig. 2). Pixels were binned to generate representative XANES spectra for each Fe-rich region. This was done using PCA/cluster analysis in Mantis (Lerotic et al., 2004), after spectra normalisation and background correction. The Fe L_3-edge peaks (L_{3a} L_{3b}; Fig. 2) on XANES spectra contain information on the oxidation state and coordination environment of Fe-rich particulates (van Aken and Liebscher, 2002; von der Heyden et al., 2012; Toner et al., 2015). Fe speciation was characterised by the difference between the ΔeV (between L_3-edge peaks) and intensity ratio of the

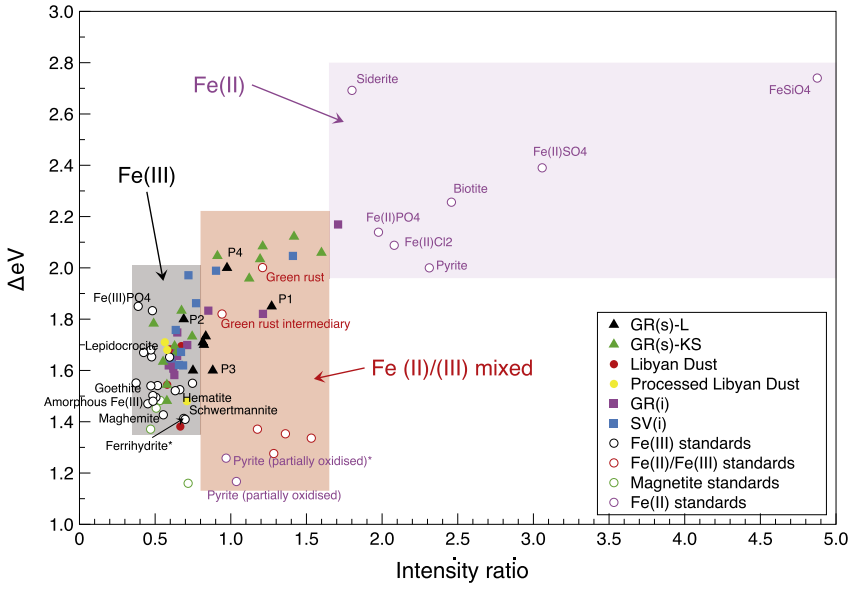

Fig. 3. Fe speciation map of ΔeV vs intensity ratio of Fe rich particles. Each XANES spectra generated for a particle are given a corresponding data point. Approximate fields for Fe(III), mixed Fe(II)/(III) and Fe(II) species are shown by the coloured boxes. Further information on standards used can be found in Table S1. * = standard spectra measured in this study. XANES spectra in Fig. 2a are labelled P1–P4.

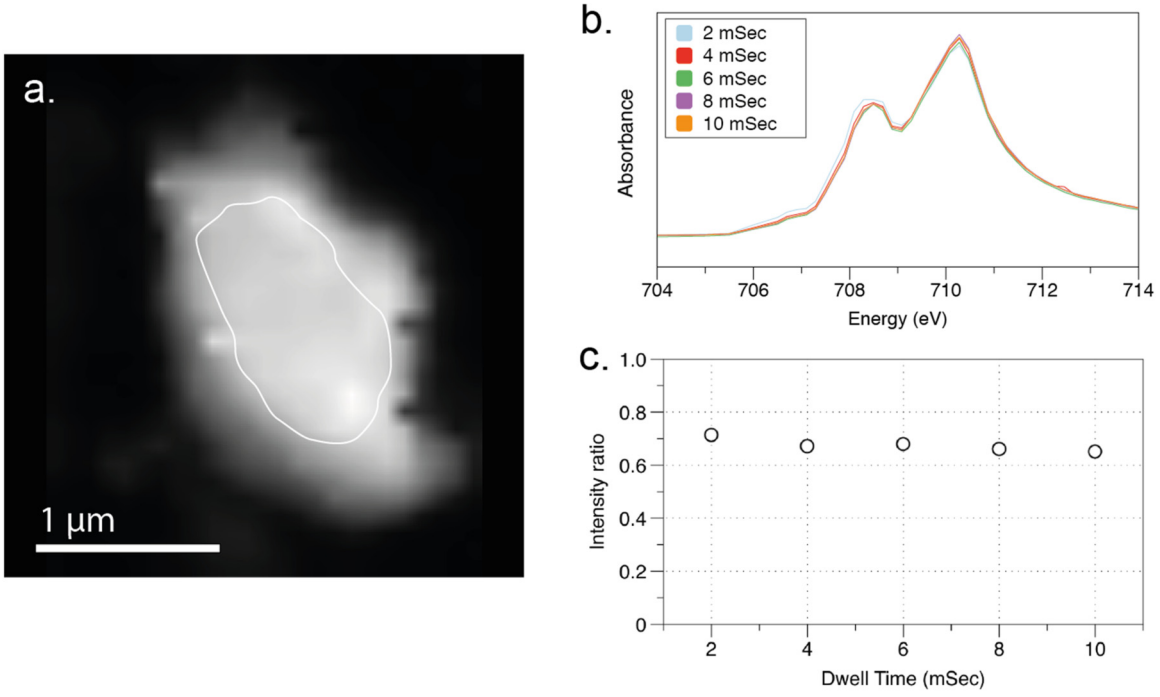

Fig. 4. Beam damage test on an Fe-rich particle. (a) Particle on which beam damage experiment was performed, (b) spectra of highlighted area in (a) after 2–10 ms of beam exposure, and (c) observed intensity ratio changes over duration of experiment.

two L_3-edge peaks (Figs. 2 and 3) (von der Heyden et al., 2012, 2014). The distribution of Fe(III) and Fe(II) species in such plots is still uncertain, and we only used standard spectra data generated via similar SXM methodologies to determine the regions of Fe(II)-rich, Fe(III)-rich and mixed valence Fe. A nominal cut off intensity ratio ~0.8 was used to differentiate between Fe(III)-rich and mixed Fe(III)/Fe(II) species, based on the Fe(III) standards measured. A linear combination fitting of each spectra was performed using the ATHENA/DEMETER (Ravel and Newville, 2005) data analysis package against the ferrihydrite and biotite spectra of Toner et al. (2009), and the ferrihydrite standard spectra acquired during our work, to generate best possible Fe(III):∑Fe ratios for all samples.

A common concern in this type of analyses is that beam damage can induce a valence shift from Fe(III) to Fe(II) (Gloter et al., 2004). We do not believe this occurred during our experiments. Beam sensitivity studies of material both using SXM and EELS showed no observable change in valence state over exposure times similar to that used to acquire spectra, in agreement with similar sensitivity experiments by others (von der Heyden et al., 2012; Bourdelle et al., 2013). Beam damage was assessed by evaluating changes to a Fe-rich particle over the 705–715 eV Fe L-edge with increasing dwell times, from 2 ms to 10 ms in 2 ms increments (Fig. 4). No significant changes in the Fe L-edge spectra or intensity ratio were observed over dwell times similar or exceeding those used in this study.

2.5. HR-TEM/EDS/EELS analysis

The morphology, structure and crystallinity of phases, but with particular focus on Fe (oxy)hydroxides, were investigated using a high-resolution field emission gun transmission electron microscopy (FEGTEM) operated at 200 kV, as per Hawkings et al. (2014). Samples dispersed in ethanol and pipetted onto holey carbon support films and particles were imaged at high-resolution. The elemental composition of nanoparticles and nanoparticle aggregates identified using HR-TEM was assessed by energy dispersive X-ray spectroscopy (EDS; Oxford Instruments) to determine the elemental characteristics of identified Fe nanophases. Selected area electron diffraction (SAED) were also taken to evaluate the crystallinity of the nanoparticles. Electron energy loss spectroscopy (EELS) was performed on amorphous or poorly crystalline nanoparticulate aggregates. EELS spectra were calibrated to the Fe(II) (707.8 eV) and Fe(III) (708.9 eV) maxima of van Aken and Liebscher (2002). Quantification of the Fe(III):$\sum$Fe ratio in nanoparticulate aggregates identified using HR-TEM and analysed using EELS was determined using the fitting method of van Aken and Liebscher (2002). Combining XANES and HR-TEM EELS analyses allowed us to quantitatively assess Fe(II):Fe(III) ratios. These data were supplemented by bulk wet-chemical extraction data (see below; Hawkings et al., 2014; Raiswell et al., 2016).

2.6. Wet chemical extractions

Well characterised ascorbate (FeA) and dithionite (FeD) wet chemical extractions were performed to determine the concentrations of highly reactive ferrihydrite and more crystalline nano-(oxy)hydroxides (aged ferrihydrite, goethite, hematite and lepidocrocite) in sediments (Raiswell et al., 2010, 2016). These extraction procedures are well documented elsewhere (Raiswell et al., 2010, 2016). Briefly, 20–40 mg of sediment was accurately weighed into a 15 mL plastic centrifuge tube, and extracted in 10 mL of a deoxygenated ascorbic acid solution buffered to pH 7.5 (0.17 M sodium citrate and 0.6 M sodium bicarbonate to which ascorbic acid was added until a pH of 7.5 was reached) for 24 h to determine FeA (highly reactive amorphous Fe nanoparticles). Following filtration through a 0.45 µm membrane, the residual sediment was extracted in 10 mL of a dithionite solution buffered to a pH of 4.8 (0.29 M sodium dithionite in 0.35 M acetic acid and 0.2 M sodium citrate) for 2 h to determine FeD (aged ferrihydrite, goethite, hematite and lepidocrocite). Solutions were analysed on an Atomic Absorption Spectrometer (Analytik Jena High-Resolution Continuum Source, ContrAA 700) with matrix matched standards.

3. Results and discussion

3.1. Chemical composition and speciation of particulate iron

All samples were fine grained, but iceberg sediments visually exhibited a larger size range, likely due to direct basal freeze-on processes at the bedrock-ice interface, which precludes fluvial sorting. In most cases, Fe-rich phases appeared to be present in nanoparticulate aggregates ~50–200 nm in size (e.g. Figs. 2a and 5) (Hawkings et al., 2014). The valence state and coordination environment of most glacially derived particulates does not match typical Fe SXM characteristics from the literature (Fig. 3). The presence of poorly ordered but mixed Fe(II)/Fe(III) nanoparticle aggregates in glacial samples (Figs. 2 and 3) with impurities (e.g., Al and Si elemental peaks are evident from EDS spectra; Figs. 2e and 5) complicates the interpretation in glacial samples.

There is a large variation in the speciation and coordination environment both within and between glacial sediment samples (Fig. 3). Variation within samples reflects a complex mix of both primary minerals (e.g. biotite and Fe(II)-silicates) and secondary-weathering products, consistent with poorly weathered, freshly crushed and ground bedrock characteristic of glacial sediments (Schroth et al., 2009; Hawkings et al., 2014). Both iceberg sediment and meltwater suspended sediments contain a wide range of Fe phases, from small Fe(II) mineral fragments <1 µm in size with biotite-like spectra (Fig. 3), to aggregates of Fe (III) oxyhydroxide nanoparticles, which resemble ferrihydrite and/or nano-crystalline goethite/hematite, as previously identified (Fig. 5) (Raiswell, 2011; Hawkings et al., 2014). HR-TEM photomicrographs (Fig. 5) and bulk sediment extractions (Table 1) confirmed the presence Fe-rich amorphous secondary weathering products, and Fe(III)-rich oxyhydroxides. Nanoparticulate clusters identified using HR-TEM photomicrographs were Fe(II)-rich and ubiquitous across glacial samples analysed, as revealed by EELS (Fig. 2d, Fig. 6b).

In contrast, both unprocessed and processed (to simulate cloud processing) aeolian dust Fe spectra plot closely to known Fe(III) standards, such as Fe(III) goethite and hematite standards (Fig. 3). This indicates little change to valence state after cloud processing, despite a possible increase in extractable Fe oxyhydroxides. This is consistent with the relatively low concentrations of extractable amorphous or poorly ordered Fe phases (e.g. ferrihydrite; FeA) in the dust samples, but their relatively high concentrations of crystalline Fe (oxy)hydroxides (FeD; Table 1) (Shi et al., 2012, 2015; Raiswell et al., 2016), which is indicative of a ferric iron dominated source and a limited bioavailability of dry deposition atmospheric dust. The XANES spectra and Fe(III):$\sum$Fe obtained in simulated atmospheric processed samples were not significantly different to the unprocessed sample (Figs. 3 and 6a; independent T-test $P > 0.1$), indicating no change to valence state after cloud processing, despite a possible increase in FeA/FeD. This provides further evidence that dust deposition is likely to provide Fe(III) rich particles to ocean sources (Lam et al., 2012), also corroborating the low concentrations of extractable amorphous Fe phases, but high crystalline Fe (oxy)hydroxide concentrations measured in these samples (Table 1) (Shi et al., 2012, 2015; Raiswell et al., 2016). These results are indicative of highly weathered and oxidised particles, and consistent with low solubility in seawater (Schroth et al., 2009).

3.2. Differences in sample composition due to particulate Fe source

Of the 22 averaged XANES spectra acquired for glacial suspended sediment particles, ~60% were mixed phase, while ~40% were Fe(III) rich (Fig. 3). In comparison, of the 22 averaged spectra acquired for iceberg particulates ~60% were Fe(III)-rich and ~40% mixed phase. HR-TEM and EELS revealed Fe(II)-rich poorly ordered nanoparticulate aggregates in all glacial samples. Photomicrographs (Figs. 2c and 5) revealed amorphous and poorly crystalline nanoparticles akin to ferrihydrite (Hawkings et al., 2014), yet XANES and EELS spectra of such particles were characterised by a significant Fe(II) component (Figs. 3 and 6). A higher proportion of mixed phase particles (75%) were observed in GR(s)-L XANES spectra compared to GR(s)-KS meltwater suspended sediments (43%), and iceberg sediments (25% for GR(i) and 22% for SV(i)), which is consistent with the lower FeA concentration determined by chemical extraction (Raiswell et al., 2010) (Figs. 3 and 6a; Table 1). This is interesting, as the source for the GR(s)-L sample, Leverett Glacier, is a relatively large glacial system (~600 km^2 in area and ~80 km in length, versus ~36 km^2 in area and ~16 km in length for Kiattuut Sermiat (Hawkings et al., 2016)) on broadly similar bedrock to Kiattuut Sermiat (Precambrian shield; Table 1). Large glacial systems are hypothesised to deliver subglacial waters (and therefore sediments) with longer residence time and from regions of potential anoxia (Wadham et al., 2010; Hawkings et al., 2014, 2016), compared to the far smaller

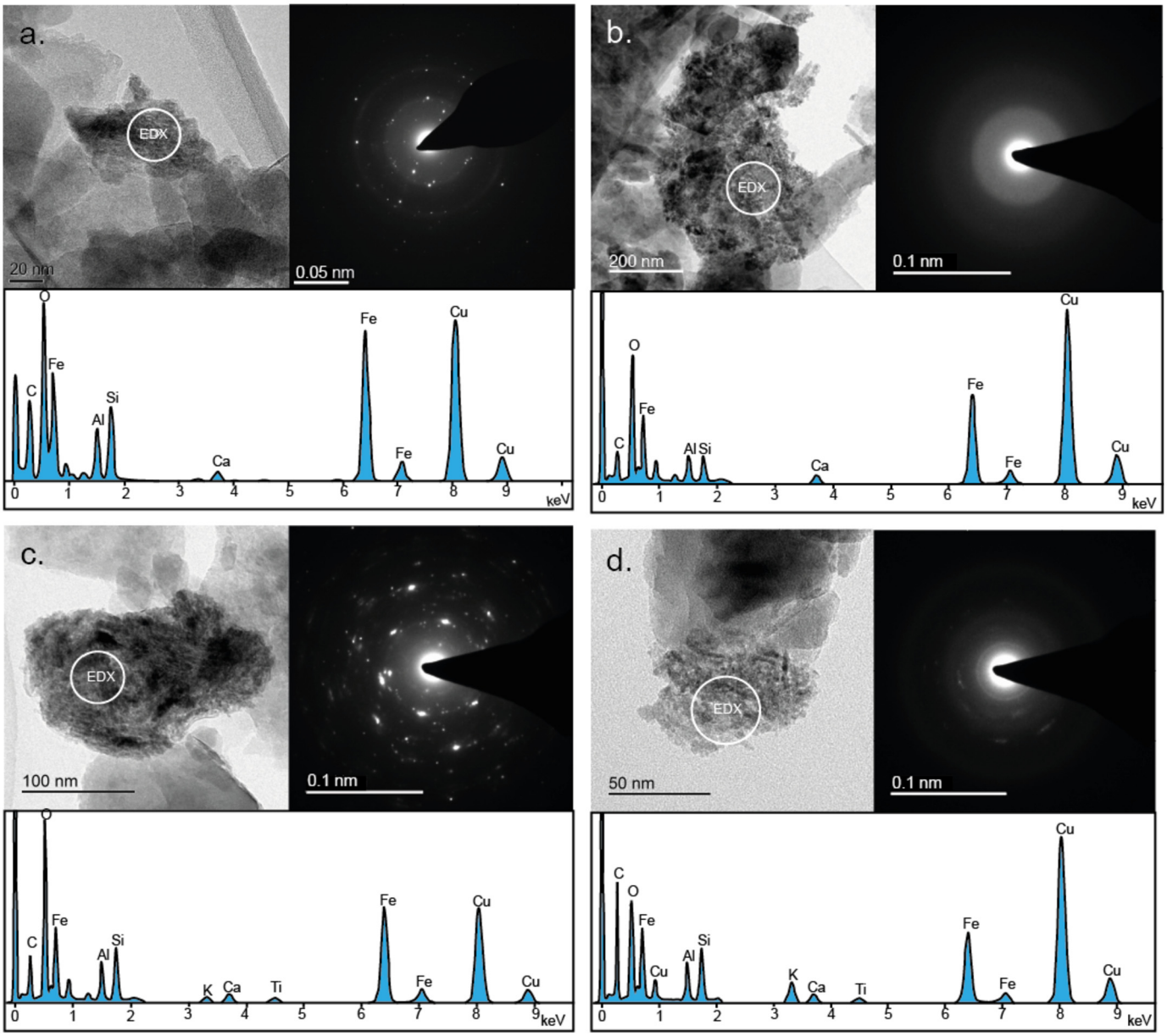

Fig. 5. Photomicrographs of Fe-rich nanoparticulate aggregates in glacial sediment samples, with associated diffraction signal and EDS spectra, from (a) Leverett Glacier suspended sediment (GR(s)-L), (b) Svalbard iceberg sediment (SV(i)), (c) Greenland iceberg sediment (GR(i)) and (d) Kiattuut Sermiat suspended sediment (GR(s)-KS).

Table 1
Ascorbate (FeA; selective for highly reactive amorphous Fe nanoparticles, e.g. 2-line ferrihydrite) and dithionite (FeD; selective for crystalline Fe nanoparticles, e.g. goethite and hematite) extraction data for samples. Results are expressed as percentage dry weight.

Sample	Samples	Regional geology	FeA (%)	FeD (%)	Reference
Leverett Glacier – GR(s)-L	33	Orthogneiss/granite; Precambrian shield	0.15 ± 0.02	0.38 ± 0.06	Hawkings et al. (2014)
Kiattuut Sermiat – GR(s)-KS	27	Granitic, with diorite-/pyroxene–biotite and basaltic intrusions; Precambrian shield	0.07 ± 0.02	0.22 ± 0.05	This study
Greenland iceberg – GR(i)	9	Orthogneiss, possibly metasedimentary/ Metavolcanic; Precambrian shield	0.04 ± 0.01	0.34 ± 0.15	Raiswell et al. (2016)
Svalbard iceberg – SV(i)	9	Metamorphosed basement rock (marbles/mica-schists), sandstones, shales, carbonates	0.13 ± 0.10	0.42 ± 0.21	Raiswell et al. (2016)
Libya dust	2	Saharan dust, dried water course	0.02 ± 0.01	1.67 ± 0.19	Shi et al. (2012)

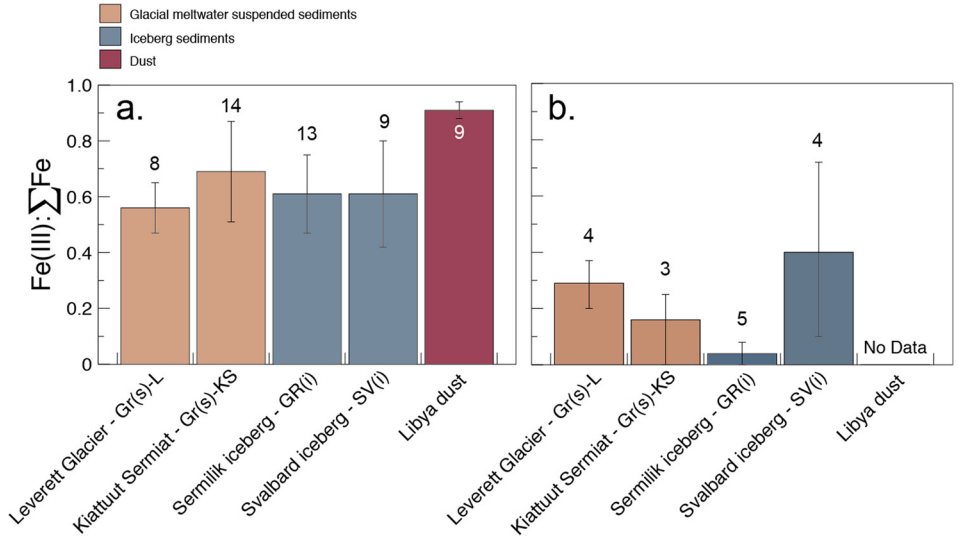

Fig. 6. Fe(III):∑Fe ratios. (a) Ratios derived from XANES, derived from a semi-quantitative fit based on Fe(II) biotite spectra and Fe(III) ferrihydrite spectra from Toner et al. (2009) as end members. Note spectra do not identically match the Fe(II) and Fe(III) standards used. (b) Ratios derived from nanoparticulate aggregates identified using HR-TEM and analysed using EELS, derived using the fitting method of van Aken and Liebscher (2002). Bar graphs in (a) and (b) are expressed as the proportion of Fe(III) analysed in each sample, with higher bars indicating a greater proportion of Fe(III) relative to Fe(II). Error bars indicate the spread of particulate spectra found, and values assigned to bars indicate the number of particles analysed in each sample. The Libya dust includes atmospherically processed samples (no data was acquired using EELS), with tight clustering of Fe(III):∑Fe ratios (i.e. little deviation in the Fe(III):∑Fe ratio).

glacial catchment from where GR(s)-KS was collected (Kiattuut Sermiat).

The main variation in XANES spectra occurs between the two L_3-edge peaks (L_{3a} and L_{3b}; Fig. 2b). The Fe(III):∑Fe ratio is highly correlated ($R^2 = 0.96$) to the intensity ratio of these two peaks in a number of standards (Bourdelle et al., 2013). We used reference XANES spectra for pure Fe(III) ferrihydrite and Fe(II) (biotite) from Toner et al. (2009) to derive a semi-quantitative Fe(III):∑Fe ratio in our Fe particulates (van Aken and Liebscher, 2002; Bourdelle et al., 2013). Our results indicate that all the glacial Fe particulates are richer in Fe(II) species (Fig. 6a) compared to our aeolian dust precursor (including atmospherically processed samples), with suspended sediments generally having a greater proportion of Fe(II) (Fig. 6a). This broadly corroborates the Fe(III):∑Fe ratios derived from EELS spectra (Fig. 6b), which show several Fe(II)-rich amorphous nanoparticulate aggregates in all glacial samples (e.g. Fig. 2). Note however that there is a large difference between the Fe(III):∑Fe ratio of samples measured using XANES (mean values 0.59–0.61) and EELS (mean values 0.04–0.40). This difference is likely related to some sampling bias using HR-TEM/EELS based analyses, targeting only obvious clusters of Fe-rich amorphous nanoparticulate material identified using HR-TEM, rather than all Fe-rich particles using the larger spatial area analysed with XANES.

GR(s)-L particles contained the highest proportion of Fe(II), according to XANES spectra (Fig. 6a), consistent with Leverett Glacier sediments containing the highest ascorbate-extractable Fe concentration of these samples (0.15 dw%; Table 1), indicative of highly reactive ferrihydrite-like Fe nanoparticles (Raiswell et al., 2010). A likely explanation for this could be the subglacial hydrological characteristics of GR(s)-L (see above discussion), as the bedrock is arguably the least reactive of all samples analysed (orthogneiss/granitic; Table 1). Iceberg sediments also had a lower Fe(III):∑Fe ratio than the dust sample, likely reflecting a hypoxic subglacial weathering environment from which they originated and/or the higher predominance of Fe(II) rich silicates from poorly weathered bedrock (Schroth et al., 2009; Shoenfelt et al., 2017). The iceberg samples also had a higher FeA concentration than the dust sample (Table 1). All dust XANES spectra plot in the Fe(III)-rich region of Fig. 4, the majority plotting closely to hematite and goethite standards (Fe oxides). The highest Fe(III):∑Fe ratios, found in unprocessed and atmospheric processed Libyan dust, is consistent with other studies (Lam et al., 2012) and precludes to its origin and oxidative atmospheric processing, while the trend to lower Fe(III):∑Fe ratios from GR(s)-KS to GR(s)-L matches the potential for greater exposure to anoxicity during subglacial weathering and the existence of poorly weathered and finely ground Fe(II) rich silicates (Figs. 4 and 5) (Schroth et al., 2009; Shoenfelt et al., 2017).

Our data suggest that the poorly ordered Fe(II) bearing mixed-phase nanoparticles may be relatively common in glacial sediments, even when sampled from oxygenated meltwaters. Mixed phase nanoparticulate Fe(II)-bearing material has only been observed in one other study (Gloter et al., 2004) to our knowledge, and the preservation mechanism was unknown.

3.3. Preservation pathways of Fe(II) in glacial sediments

The presence of a relatively high proportion of ferrous iron in the poorly ordered nanoparticle aggregates from glacial and iceberg samples is intriguing. Previous studies have suggested organic carbon complexation stabilises Fe(II) in particles sampled from oxygenated waters (Toner et al., 2009; von der Heyden et al., 2014). We believe this is unlikely in glacial sediments, which generally have very low concentrations of organic carbon (<0.1% by weight) (Hopwood et al., 2014; Lawson et al., 2014). Previous work also found no significant correlation between the concentrations of highly reactive iron and organic carbon concentration in glacial sediments (Hopwood et al., 2014).

We propose that Fe(II) in the analysed nanoparticle aggregates were likely stabilised by inorganic species, such as amorphous silica (Hawkings et al., 2017), possibly via surface complexation of dissolved Fe(II) onto hydroxyl groups (Hofstetter et al., 2003). Silica has a high affinity to nanoparticulate Fe minerals, such as ferrihydrite and green rust, and is known to inhibit aging effects and promote structural disorder (Parfitt et al., 1992; Swedlund and Webster, 1999; Kwon et al., 2007; Christiansen et al., 2009; Wang et al., 2018). Amorphous silica is present at high concentrations in glacial sediments (Hawkings et al., 2017) and silicon

peaks identified with Fe rich material using EDS analyses (Figs. 2e and 5) (Hawkings et al., 2014), may represent amorphous silica distributed within Fe-rich nanoparticle aggregates. A relationship between amorphous silica and Fe(II) has also been observed elsewhere. For example, ferrous Fe was observed to be stabilised within the amorphous silica of biogenic opal in the Southern Ocean (Ingall et al., 2013).

If the Fe(II) observed in the amorphous nanoparticulate aggregates (Figs. 2, 3 and 6) is not on the particle surface, then it may only be necessary to stabilise the amorphous Fe structure (previously believed to be ferrihydrite). Alteration of amorphous Fe nanoparticles to more crystalline Fe (oxy)hydroxides takes several years at low temperatures (Raiswell and Canfield, 2012; Raiswell et al., 2016), and this can be extended by adsorbed ions, organic ligands, silica (as above) and bacteria (Kennedy et al., 2004). Clearly, more work is needed to establish the prevailing Fe(II) preservation mechanisms in natural samples.

3.4. Implications for the export of biolabile particulate Fe from ice sheets

Our findings add crucial corroboration and mineralogical detail to earlier studies of reactive iron in glacial flours and dusts (Schroth et al., 2009; Hawkings et al., 2014; Hopwood et al., 2014; Raiswell et al., 2016; Shoenfelt et al., 2017). The existence of Fe(II)-rich particles in glacial samples demonstrates high lability and therefore potential bioavailability, due to the thermodynamic instability of Fe(II) (Schroth et al., 2009; Lam et al., 2012; Oakes et al., 2012; Shaked and Lis, 2012) and the ability of marine microbiota to more efficiently mine Fe(II) than Fe(III) from particulates (Rubin et al., 2011; Shoenfelt et al., 2017). We postulate potentially bioavailable Fe phases are likely to remain in suspension in the euphotic zone of near marine ecosystems for extended periods of time, which increases the likelihood of biological utilisation and transport. Sinking rates depend on particle size, which is in turn affected by scavenging, coagulation and flocculation (Raiswell and Canfield, 2012; Markussen et al., 2016). For ~2 μm particles (approximately the size of particulates analysed in this study) these sinking rates are broadly comparable to dissolution rates for ferrihydrite (<0.1 m day^{-1}), and slower than grazing and photoreduction (Raiswell and Canfield, 2012). Furthermore, glacial particulate matter has been observed to form buoyant flocs on contact with salt water, which is thought to extend residence time in surface waters and increase horizontal transport over salinity gradients (Schroth et al., 2014; Markussen et al., 2016).

Recent work indicates that the large summer phytoplankton bloom off the south–west of Greenland, responsible for nearly 50% of annual productivity in the region, is likely stimulated by the arrival of Fe from Greenland Ice Sheet meltwaters (Arrigo et al., 2017). Here we provide evidence that glacially derived particulate Fe contains a large Fe(II) fraction (~40%; Fig. 6), which is potentially bioavailable to phytoplankton in this highly productive region of the Labrador Sea. There are clear limitations in using four glacial samples to estimate the prevalence of potentially bioavailable mixed valence nanoparticle Fe in glacial sediments at large, and the capacity of glacial Fe to fertilise near coastal ecosystems. However, all glacial samples measured, from four spatially different locations, exhibit Fe(II) bearing particles (22–75% of particles are mixed phase or Fe(II)-rich), which corroborates other evidence of Fe(II) in glacial sediments (Schroth et al., 2009; Hopwood et al., 2014; Shoenfelt et al., 2017), and studies indicating Fe-derived from glacial meltwaters and iceberg rafted debris stimulates productivity in downstream Fe-limited regions of the ocean (Smith et al., 2007; Gerringa et al., 2012; Duprat et al., 2016; Raiswell et al., 2016; Monien et al., 2017).

The subglacial drainage system under the Antarctic Ice Sheet is characterised by high rock to water ratios, and long meltwater residence times (Mikucki et al., 2009; Wadham et al., 2010; Michaud et al., 2016). It is therefore likely that similar biogeochemical processes to what we observe in large Greenlandic catchments, like Leverett Glacier, may be occurring under the larger Antarctic Ice Sheet, where parts of the subglacial environment are likely hypoxic or anoxic and have the capacity to generate high dissolved Fe^{2+} concentrations (Mikucki et al., 2009; Wadham et al., 2010; Michaud et al., 2016; Nixon et al., 2017). Recent research points to significant outflow of subglacial freshwater from the Antarctic Ice Sheet to the Southern Ocean (Le Brocq et al., 2013; Garabato et al., 2017), a potential mechanism of substantial Fe-rich meltwater export. Our results therefore also suggest a potential glacial source of the Fe(II) rich particles found near the coast of Antarctica (von der Heyden et al., 2012), directly downstream of the Julutstramen ice stream outflow, which is associated with a region of high productivity. However, we acknowledge that uncertainties based on data from Arctic glaciers is large. Our knowledge of these remote environments is currently limited due to sampling difficulties, and there is a need to further test this hypothesis.

4. Conclusions

Using a suite of high resolution microscopic and spectroscopic techniques we have demonstrated that glacial meltwater suspended sediments and iceberg hosted sediments from the Arctic harbour potentially bioavailable Fe(II)-rich nanoparticles. Fe(II) bearing nanoparticles are present in all glacial sediments sampled, yet an unprocessed and atmospherically processed aeolian dust sample contained only Fe(III)-rich particles. These differences in speciation will likely will dictate bioavailability of particles on delivery to marine ecosystems, with Fe(II) bearing particles having higher biolability (Shoenfelt et al., 2017). Our findings have important implications for assessing the importance of particulate material delivered to the polar oceans, especially in regions where iron potentially limits primary production and therefore CO_2 drawdown (Arrigo et al., 2017). We propose that Fe quality rather quantity will likely be critically important in assessing the importance of contributions from different Fe sources, and that glaciers deliver significant quantities of biolabile Fe(II)-containing amorphous nanoparticles to downstream ecosystems.

Acknowledgements

This work was carried out with the support of the Diamond Light Source under the proposal SP11016 awarded to L.G.B. and J.R.H. We also acknowledge the contributions of UK NERC funded DELVE (NERC grant NE/I008845/1) to J.L.W., and the Arctic Soils grant (NERC grant NE/J022365/1) to L.G.B. We thank all of those who assisted with fieldwork at Leverett Glacier and Kiattuut Sermiat, as well as Dr. Mike Ward at the LEMAS facility in the University of Leeds and Dr. Richard Wirth at GFZ Potsdam.

Author contributions

All authors made significant contributions to the research presented here. J.R.H., L.G.B. and R.R. conceived the project. J.R.H., R.R. and L.G.B. collected the samples. J.R.H., L.G.B., R.R., B.K., T.A., M.A. and A.S. undertook lab analysis. M.K.-M. helped with data processing, and J.L.W. and M.T. assisted with data interpretation. J.R.H. wrote the manuscript with contributions for all authors.

Competing interests

The authors declare no competing interests.

Appendix A. Supplementary material

Supplementary material related to this article can be found online at https://doi.org/10.1016/j.epsl.2018.04.022.

References

Annett, A.L., Fitzsimmons, J.N., Séguret, M.J.M., Lagerström, M., Meredith, M.P., Schofield, O., Sherrell, R.M., 2017. Controls on dissolved and particulate iron distributions in surface waters of the Western Antarctic Peninsula shelf. Mar. Chem. 196, 81–97.

Arrigo, K.R., van Dijken, G.L., Castelao, R.M., Luo, H., Rennermalm, Å.K., Tedesco, M., Mote, T.L., Oliver, H., Yager, P.L., 2017. Melting glaciers stimulate large summer phytoplankton blooms in southwest Greenland waters. Geophys. Res. Lett. 44, 6278–6285.

Bhatia, M.P., Kujawinski, E.B., Das, S.B., Breier, C.F., Henderson, P.B., Charette, M.A., 2013. Greenland meltwater as a significant and potentially bioavailable source of iron to the ocean. Nat. Geosci. 6, 274–278.

Bourdelle, F., Benzerara, K., Beyssac, O., Cosmidis, J., Neuville, D.R., Brown, G.E., Paineau, E., 2013. Quantification of the ferric/ferrous iron ratio in silicates by scanning transmission X-ray microscopy at the Fe L2, 3 edges. Contrib. Mineral. Petrol. 166, 423–434.

Breitbarth, E., Gelting, J., Walve, J., Hoffmann, L.J., Turner, D.R., Hassellov, M., Ingri, J., 2009. Dissolved iron (II) in the Baltic Sea surface water and implications for cyanobacterial bloom development. Biogeosciences 6, 2397–2420.

Christiansen, B.C., Balic-Zunic, T., Dideriksen, K., Stipp, S.L.S., 2009. Identification of green rust in groundwater. Environ. Sci. Technol. 43, 3436–3441.

Death, R., Wadham, J.L., Monteiro, F., Le Brocq, A.M., Tranter, M., Ridgwell, A., Dutkiewicz, S., Raiswell, R., 2014. Antarctic ice sheet fertilises the Southern Ocean. Biogeosciences 11, 2635–2643.

Duprat, L.P.A.M., Bigg, G.R., Wilton, D.J., 2016. Enhanced Southern Ocean marine productivity due to fertilization by giant icebergs. Nat. Geosci. 9, 219–221.

Frisia, S., Weyrich, L.S., Hellstrom, J., Borsato, A., Golledge, N.R., Anesio, A.M., Bajo, P., Drysdale, R.N., Augustinus, P.C., Rivard, C., Cooper, A., 2017. The influence of Antarctic subglacial volcanism on the global iron cycle during the Last Glacial Maximum. Nat. Commun. 8, 15425.

Garabato, A.C.N., Forryan, A., Dutrieux, P., Brannigan, L., Biddle, L.C., Heywood, K.J., Jenkins, A., Firing, Y.L., Kimura, S., 2017. Vigorous lateral export of the meltwater outflow from beneath an Antarctic ice shelf. Nature 542, 219–222.

Gerringa, L.J.A., Alderkamp, A.C., Laan, P., Thuroczy, C.E., De Baar, H.J.W., Mills, M.M., van Dijken, G.L., van Haren, H., Arrigo, K.R., 2012. Iron from melting glaciers fuels the phytoplankton blooms in Amundsen Sea (Southern Ocean): iron biogeochemistry. Deep-Sea Res., Part 2, Top. Stud. Oceanogr., 71–76, 16–31.

Gloter, A., Zbinden, M., Guyot, F., Gaill, F., Colliex, C., 2004. TEM-EELS study of natural ferrihydrite from geological–biological interactions in hydrothermal systems. Earth Planet. Sci. Lett. 222, 947–957.

Hawkings, J., Wadham, J., Tranter, M., Telling, J., Bagshaw, E., Beaton, A., Simmons, S.-L., Chandler, D., Tedstone, A., Nienow, P., 2016. The Greenland Ice Sheet as a hotspot of phosphorus weathering and export in the Arctic. Glob. Biogeochem. Cycles 30, 191–210.

Hawkings, J.R., Wadham, J.L., Benning, L.G., Hendry, K.R., Tranter, M., Tedstone, A., Nienow, P., Raiswell, R., 2017. Ice sheets as a missing source of silica to the polar oceans. Nat. Commun. 8, 14198.

Hawkings, J.R., Wadham, J.L., Tranter, M., Raiswell, R., Benning, L.G., Statham, P.J., Tedstone, A., Nienow, P., Lee, K., Telling, J., 2014. Ice sheets as a significant source of highly reactive nanoparticulate iron to the oceans. Nat. Commun. 5.

Hodson, A., Nowak, A., Sabacka, M., Jungblut, A., Navarro, F., Pearce, D., Ávila-Jiménez, M.L., Convey, P., Vieira, G., 2017. Climatically sensitive transfer of iron to maritime Antarctic ecosystems by surface runoff. Nat. Commun. 8, 14499.

Hofstetter, T.B., Schwarzenbach, R.P., Haderlein, S.B., 2003. Reactivity of Fe(II) species associated with clay minerals. Environ. Sci. Technol. 37, 519–528.

Hopwood, M., Statham, P., Tranter, M., Wadham, J., 2014. Glacial flours as a potential source of Fe(II) and Fe(III) to polar waters. Biogeochemistry, 1–10.

Ingall, E.D., Diaz, J.M., Longo, A.F., Oakes, M., Finney, L., Vogt, S., Lai, B., Yager, P.L., Twining, B.S., Brandes, J.A., 2013. Role of biogenic silica in the removal of iron from the Antarctic seas. Nat. Commun. 4, 1981.

Kennedy, C.B., Scott, S.D., Ferris, F.G., 2004. Hydrothermal phase stabilization of 2-line ferrihydrite by bacteria. Chem. Geol. 212, 269–277.

Kwon, S.K., Kimijima, K., Kanie, K., Suzuki, S., Muramatsu, A., Saito, M., Shinoda, K., Waseda, Y., 2007. Influence of silicate ions on the formation of goethite from green rust in aqueous solution. Corros. Sci. 49, 2946–2961.

Lam, P.J., Ohnemus, D.C., Marcus, M.A., 2012. The speciation of marine particulate iron adjacent to active and passive continental margins. Geochim. Cosmochim. Acta 80, 108–124.

Lawson, E.C., Wadham, J.L., Tranter, M., Stibal, M., Lis, G.P., Butler, C.E.H., Laybourn-Parry, J., Nienow, P., Chandler, D., Dewsbury, P., 2014. Greenland Ice Sheet exports labile organic carbon to the Arctic oceans. Biogeosciences 11, 4015–4028.

Le Brocq, A., Ross, N., Bingham, R., Corr, H.F.J., Ferraccioli, F., Jenkins, A., Jordan, T., Payne, A.J., Rippin, D., Siegert, M., 2013. Evidence from ice shelves for channelized meltwater flow beneath the Antarctic Ice Sheet. Nat. Geosci. 6, 945–948.

Lerotic, M., Jacobsen, C., Schafer, T., Vogt, S., 2004. Cluster analysis of soft X-ray spectromicroscopy data. Ultramicroscopy 100, 35–57.

Lyons, W.B., Dailey, K.R., Welch, K.A., Deuerling, K.M., Welch, S.A., McKnight, D.M., 2015. Antarctic streams as a potential source of iron for the Southern Ocean. Geology 43, 1003–1006.

Markussen, T.N., Elberling, B., Winter, C., Andersen, T.J., 2016. Flocculated meltwater particles control Arctic land-sea fluxes of labile iron. Sci. Rep. 6, 24033.

Michaud, A.B., Skidmore, M.L., Mitchell, A.C., Vick-Majors, T.J., Barbante, C., Turetta, C., van Gelder, W., Priscu, J.C., 2016. Solute sources and geochemical processes in Subglacial Lake Whillans, West Antarctica. Geology 44, 347–350.

Mikucki, J.A., Pearson, A., Johnston, D.T., Turchyn, A.V., Farquhar, J., Schrag, D.P., Anbar, A.D., Priscu, J.C., Lee, P.A., 2009. A contemporary microbially maintained subglacial Ferrous "Ocean". Science 324, 397–400.

Monien, D., Monien, P., Brünjes, R., Widmer, T., Kappenberg, A., Silva Busso, A.A., Schnetger, B., Brumsack, H.-J., 2017. Meltwater as a source of potentially bioavailable iron to Antarctica waters. Antarct. Sci. 29, 277–291.

Moore, C.M., Mills, M.M., Arrigo, K.R., Berman-Frank, I., Bopp, L., Boyd, P.W., Galbraith, E.D., Geider, R.J., Guieu, C., Jaccard, S.L., Jickells, T.D., La Roche, J., Lenton, T.M., Mahowald, N.M., Maranon, E., Marinov, I., Moore, J.K., Nakatsuka, T., Oschlies, A., Saito, M.A., Thingstad, T.F., Tsuda, A., Ulloa, O., 2013. Processes and patterns of oceanic nutrient limitation. Nat. Geosci. 6, 701–710.

Nixon, S.L., Telling, J.P., Wadham, J.L., Cockell, C.S., 2017. Viable cold-tolerant iron-reducing microorganisms in geographically diverse subglacial environments. Biogeosciences 14, 1445–1455.

Oakes, M., Weber, R.J., Lai, B., Russell, A., Ingall, E.D., 2012. Characterization of iron speciation in urban and rural single particles using XANES spectroscopy and micro X-ray fluorescence measurements: investigating the relationship between speciation and fractional iron solubility. Atmos. Chem. Phys. 12, 745–756.

Parfitt, R.L., Vandergaast, S.J., Childs, C.W., 1992. A structural model for natural siliceous ferrihydrite. Clays Clay Miner. 40, 675–681.

Raiswell, R., 2011. Iceberg-hosted nanoparticulate Fe in the Southern Ocean: mineralogy, origin, dissolution kinetics and source of bioavailable Fe. Deep-Sea Res., Part 2, Top. Stud. Oceanogr. 58, 1364–1375.

Raiswell, R., Canfield, D.E., 2012. The iron biogeochemical cycle past and present. Geochem. Perspect. 1, 1–220.

Raiswell, R., Hawkings, J.R., Benning, L.G., Baker, A.R., Death, R., Albani, S., Mahowald, N., Krom, M.D., Poulton, S.W., Wadham, J., Tranter, M., 2016. Potentially bioavailable iron delivery by iceberg-hosted sediments and atmospheric dust to the polar oceans. Biogeosciences 13, 3887–3900.

Raiswell, R., Vu, H.P., Brinza, L., Benning, L.G., 2010. The determination of labile Fe in ferrihydrite by ascorbic acid extraction: methodology, dissolution kinetics and loss of solubility with age and de-watering. Chem. Geol. 278, 70–79.

Ravel, B., Newville, M., 2005. ATHENA, ARTEMIS, HEPHAESTUS: data analysis for X-ray absorption spectroscopy using IFEFFIT. J. Synchrotron Radiat. 12, 537–541.

Rubin, M., Berman-Frank, I., Shaked, Y., 2011. Dust- and mineral-iron utilization by the marine dinitrogen-fixer Trichodesmium. Nat. Geosci. 4, 529–534.

Schroth, A.W., Crusius, J., Chever, F., Bostick, B.C., Rouxel, O.J., 2011. Glacial influence on the geochemistry of riverine iron fluxes to the Gulf of Alaska and effects of deglaciation. Geophys. Res. Lett. 38, L16605.

Schroth, A.W., Crusius, J., Hoyer, I., Campbell, R., 2014. Estuarine removal of glacial iron and implications for iron fluxes to the ocean. Geophys. Res. Lett. 41, 3951–3958.

Schroth, A.W., Crusius, J., Sholkovitz, E.R., Bostick, B.C., 2009. Iron solubility driven by speciation in dust sources to the ocean. Nat. Geosci. 2, 337–340.

Schwertmann, U., Stanjek, H., Becher, H.H., 2004. Long-term in vitro transformation of 2-line ferrihydrite to goethite/hematite at 4, 10, 15 and 25 °C. Clay Miner. 39, 433–438.

Shaked, Y., Lis, H., 2012. Disassembling iron availability to phytoplankton. Front. Microbiol. 3.

Shi, Z., Krom, M.D., Bonneville, S., Baker, A.R., Bristow, C., Drake, N., Mann, G., Carslaw, K., McQuaid, J.B., Jickells, T., Benning, L.G., 2011. Influence of chemical weathering and aging of iron oxides on the potential iron solubility of Saharan dust during simulated atmospheric processing. Glob. Biogeochem. Cycles 25.

Shi, Z., Krom, M.D., Bonneville, S., Benning, L.G., 2015. Atmospheric processing outside clouds increases soluble iron in mineral dust. Environ. Sci. Technol. 49, 1472–1477.

Shi, Z.B., Krom, M.D., Jickells, T.D., Bonneville, S., Carslaw, K.S., Mihalopoulos, N., Baker, A.R., Benning, L.G., 2012. Impacts on iron solubility in the mineral dust by processes in the source region and the atmosphere: a review. Aeolian Res. 5, 21–42.

Shoenfelt, E.M., Sun, J., Winckler, G., Kaplan, M.R., Borunda, A.L., Farrell, K.R., Moreno, P.I., Gaiero, D.M., Recasens, C., Sambrotto, R.N., Bostick, B.C., 2017. High particulate iron(II) content in glacially sourced dusts enhances productivity of a model diatom. Sci. Adv. 3.

Smith, K.L., Robison, B.H., Helly, J.J., Kaufmann, R.S., Ruhl, H.A., Shaw, T.J., Twining, B.S., Vernet, M., 2007. Free-drifting icebergs: hot spots of chemical and biological enrichment in the Weddell Sea. Science 317, 478–482.

Sugie, K., Nishioka, J., Kuma, K., Volkov, Y.N., Nakatsuka, T., 2013. Availability of particulate Fe to phytoplankton in the Sea of Okhotsk. Mar. Chem. 152, 20–31.

Swedlund, P.J., Webster, J.G., 1999. Adsorption and polymerisation of silicic acid on ferrihydrite, and its effect on arsenic adsorption. Water Res. 33, 3413–3422.

Toner, B.M., Fakra, S.C., Manganini, S.J., Santelli, C.M., Marcus, M.A., Moffett, J.W., Rouxel, O., German, C.R., Edwards, K.J., 2009. Preservation of iron(II) by carbon-rich matrices in a hydrothermal plume. Nat. Geosci. 2, 197–201.

Toner, B.M., German, C.R., Dick, G.J., Breier, J.A., 2015. Deciphering the complex chemistry of deep-ocean particles using complementary synchrotron X-ray microscope and microprobe instruments. Acc. Chem. Res. 49, 128–137.

van Aken, P.A., Liebscher, B., 2002. Quantification of ferrous/ferric ratios in minerals: new evaluation schemes of Fe L 23 electron energy-loss near-edge spectra. Phys. Chem. Miner. 29, 188–200.

von der Heyden, B.P., Hauser, E.J., Mishra, B., Martinez, G.A., Bowie, A.R., Tyliszczak, T., Mtshali, T.N., Roychoudhury, A.N., Myneni, S.C.B., 2014. Ubiquitous presence of Fe(II) in aquatic colloids and its association with organic carbon. Environ. Sci. Technol. Lett. 1, 387–392.

von der Heyden, B.P., Roychoudhury, A.N., Mtshali, T.N., Tyliszczak, T., Myneni, S.C.B., 2012. Chemically and geographically distinct solid-phase iron pools in the Southern Ocean. Science 338, 1199–1201.

Wadham, J., De'ath, R., Monteiro, F.M., Tranter, M., Ridgwell, A., Raiswell, R., Tulaczyk, S., 2013. The potential role of the Antarctic Ice Sheet in global biogeochemical cycles. Earth Environ. Sci. Trans. R. Soc. 104, 55–67.

Wadham, J.L., Tranter, M., Skidmore, M., Hodson, A.J., Priscu, J., Lyons, W.B., Sharp, M., Wynn, P., Jackson, M., 2010. Biogeochemical weathering under ice: size matters. Glob. Biogeochem. Cycles 24, GB3025.

Wang, X., Kubicki, J.D., Boily, J.-F., Waychunas, G.A., Hu, Y., Feng, X., Zhu, M., 2018. Binding geometries of silicate species on ferrihydrite surfaces. ACS Earth Space Chem. 2, 125–134.